

UCSF

UC San Francisco Electronic Theses and Dissertations

Title

In Vivo Hyperpolarized Carbon-13 Diffusion Weighted MRI Measures Lactate Metabolism and Transport in Prostate Cancer

Permalink

<https://escholarship.org/uc/item/8cq5f3bb>

Author

Qin, Hecong

Publication Date

2015

Peer reviewed|Thesis/dissertation

In Vivo Hyperpolarized Carbon-13 Diffusion Weighted MRI
Measures Lactate Metabolism and Transport in Prostate Cancer

by

Hecong Qin

THESIS

Submitted in partial satisfaction of the requirements for the degree of

MASTER OF SCIENCE

in

Biomedical Imaging

in the

GRADUATE DIVISION

of the

UNIVERSITY OF CALIFORNIA, SAN FRANCISCO

Copyright 2015

by

Hecong Qin

*To my late grandmother who died of cancer,
and people whose life have been affected by cancer*

Acknowledgments

I am fortunate to have three great mentors during my thesis work: Drs. John Kurhanewicz, Peder Larson, and Jeremy Gordon. As my academic adviser, John has provided me with an unparalleled research opportunity in his lab. He is a true Principle Investigator, always providing directional guidance, pointing out the "thousand dollar question" and making sure I understand the big picture. Despite his busy schedule, he always makes himself available whenever I want to talk. In addition to the lab work, John has been extremely supportive of my professional development. I could not ask for a better mentor.

Peder is the instructor of BI 201, a member of my thesis committee, and the co-PI of this project. He has been a wonderful teacher and mentor to me. His magic MRI mind gradually infected me through his office hours and discussions about the project. Thank you, Peder.

Jeremy is the core of this project, without whom this thesis work is impossible. He is not only a knowledgeable scientist, but also a great teacher. I learned so much from him, from his extensive MRI knowledge to the way he handles research and work. I owe this diffusion expert an effusive thank you.

I want to express sincere gratitude to Drs. Susan Noworolski and Michael Evans for serving on my thesis committee and for the valuable advice they provided; and to Drs. Robert Bok and Renuka Sriram for assisting with the experiments and all the helpful discussions; to all my colleagues and faculties of the MSBI program for making the past year amazing.

I also thank current and formal members of the Kurhanewicz Lab, especially Drs. Bertram Koelsch and Kayvan Keshari, whose previous research is the foundation of this project.

Besides those who helped me grow as a scientist, I would like to take this opportunity to acknowledge some important people in my life who made me a better person: James Warhol, Hubert Wieckowski, Zhao Chunxu, Tao Tao, Piao Nan, and Wang Yihan.

Finally, I want to thank my parents, Qin Xuejue and Geng Shuqin, for their unconditional love, for generously supporting me to pursue science and medicine, and for making me feel cared for and protected even when I am on the other side of the globe.

In Vivo Hyperpolarized Carbon-13 Diffusion Weighted MRI Measures Lactate Metabolism and Transport in Prostate Cancer

by

Hecong Qin

Abstract: Prostate cancer is a heterogeneous group of tumors ranging from clinically insignificant to lethally malignant. The clinical management of prostate cancer is challenging due to the lack of accurate assessment of cancer aggressiveness. Hyperpolarized magnetic resonance imaging (MRI) has enabled real-time measurement of metabolism, and has shown great promise for cancer diagnosis, staging and assessing therapeutic response in both pre-clinical and clinical studies. Aggressive prostate cancer overproduces lactate and overexpresses MCT4, the transporter primarily responsible for lactate efflux, resulting in acidification of the extracellular space and conferring a poor prognosis. In this pilot study, hyperpolarized diffusion weighted MRI was used to elucidate the intra and extracellular distribution of metabolites, which can infer lactate efflux, and tumor microstructural environment. Transgenic adenocarcinoma mouse prostate (TRAMP) models of different stages were injected with hyperpolarized pyruvate; then pyruvate and lactate were excited with a single-band spectral-spatial RF pulse, followed by a single-shot, double spin-echo flyback echo planar imaging (EPI) readout. Four b-values were acquired per metabolite, ranging from $25\text{-}1000\text{ s} \cdot \text{mm}^{-1}$. Data were corrected for RF utilization and fit voxel-wise to a monoexponential decay to generate apparent diffusion coefficient (ADC) maps for each metabolite. We found that the *in vivo* lactate ADC is close to the *ex vivo* extracellular ADC, rather than the intracellular ADC. We also found lactate ADC in late-stage tumors ($0.65 \pm 0.11\text{ mm}^2 \cdot \text{s}^{-1}$, n=4) is higher than early-stage ($0.46\text{ mm}^2 \cdot \text{s}^{-1}$, n=1), indicating there is increased lactate efflux in aggressive cancer. In conclusion, we demonstrated that hyperpolarized diffusion weighted MRI can provide insight into metabolite compartmentalization and lactate efflux in the prostate tumor, and potentially assess cancer aggressiveness and therapeutic changes in a rapid, non-invasive manner.

Contents

Acknowledgments	iv
Abstract	v
Contents	vi
List of Figures	viii
List of Tables	ix
1 Introduction	1
2 Imaging Theory	5
2.1 Magnetic Resonance	5
2.2 Hyperpolarized MR	7
2.3 Diffusion and Diffusion MR	7
3 Methods	9
3.1 Hardware	9
3.2 Hyperpolarization	9
3.3 Animal Experiment and Scan Protocol	10
3.4 ^1H Imaging	10

3.5	Hyperpolarized ^{13}C Diffusion Weighted Imaging	11
3.6	Data Analysis	12
4	Results	14
5	Discussion	21
6	Conclusion	25
	Bibliography	26

List of Figures

3.1	Hyperpolarized ^{13}C Diffusion MR pulse sequence diagram	12
4.1	^{13}C MR spectroscopy of the imaging slab	15
4.2	Diffusion weighted images of lactate	15
4.3	Diffusion weighted images of pyruvate	15
4.4	Overlay of metabolite ADC maps and T2 weighted anatomy images	17
4.5	Histogram of Metabolite ADC maps	17
4.6	Fitting Quality of Metabolite ADC	18
4.7	A case analysis on the effect of morphology on metabolite diffusivity: histogram of ADC maps.	19
4.8	Proton ADC map and its histogram	20

List of Tables

4.1	<i>in vivo</i> effective ADC of metabolites in the prostate tumor	18
4.2	Metabolite ADC comparison: <i>in vivo</i> vs. bioreactor	18
4.3	Metabolite ADC comparison: the effect of tumor morphology	19
4.4	<i>In vivo</i> metabolite ADC measured without the lowest b-value	20

Chapter 1

Introduction

Disease Background

Prostate cancer is a major health concern in the United States. It is the most frequently diagnosed non-cutaneous cancer and the second-leading cause of cancer death among men, with an estimated 221,000 cases and 27,500 deaths in 2015 [1]. Based on data from 2010 to 2012, the lifetime risk of developing prostate cancer for U.S. men is approximately 14% [2]. Moreover, there are an estimated 2.7 million men living with prostate cancer in the United States [2]. The prostate cancer incidence has been rising since the 1980s, which is correlated with the implementation of the Prostate Specific Antigen (PSA) test. This "overdiagnosis" has caused benign and indolent prostate cancer is detected early and subsequently treated with unnecessary aggressive approach [3].

The most characteristic feature of prostate cancer, perhaps, is its diverse range of clinical behaviors, from clinically insignificant to lethally malignant. Despite high overall incidence and mortality, more than half of prostate cancers are localized, non-life-threatening and do not need radical treatments, as evidenced by the 5-year survival rate being almost 100% [4]. That being said, prostate cancer is not a trivial disease. For distant stage prostate cancer, in which cancer spreads to distant lymph nodes and other organs, the 5-year survival rate can be as low as 28% [4]. Therefore, it is crucial to distinguish aggressive cancers that will potentially metastasize from indolent cancers that may never be clinically significant, and

choose the appropriate management strategy based on the biological characteristics and the aggressiveness of the cancer [5].

However, the current risk assessment methods for prostate cancer are often unreliable and rely heavily on biopsy, which is invasive and mainly provides limited morphological information on local lesions. As a result, even though there are an estimated over 100,000 patients who are candidates for active surveillance per year in the United States, more than 90% of patients receive immediate treatment after diagnosis, as there are no accurate diagnostic tools to evaluate and monitor cancer aggressiveness [6]. Moreover, the aggressive treatments suffer from unwanted but unavoidable complications, such as urinary incontinence and sexual impotence. These complications are debilitating to prostate cancer patients who are generally over 65-years of age and tend not to die from the cancer itself.

Motivation and Significance

This project is motivated by the need for a new prostate cancer imaging method that can noninvasively assess cancer biological behaviors, provide accurate cancer risk assessment, and guide disease management of cancer. Accurate assessment of cancer aggressiveness can help identify a personalized management strategy, and encourage active surveillance candidates to stay with follow-up. From the health economics perspective, it has been estimated that patients following active surveillance can lead to considerable medical cost savings relative to those receiving immediate treatment [7].

Biological Rationale

Lactate, the primary byproduct of glycolysis, has been reported to play an critical role in cancer development [8]. The famous *Warburg effect* states that cancer cells prefer glycolysis, even in the presence of oxygen [9]. Although glycolysis is inefficient in producing ATP compared to oxidative phosphorylation, this metabolic change is critical in cancer development. The excessive proliferation of cancer cells can cause hypoxia in local tissues;

thus, cancer cells need to adapt to the new microenvironment [10]. Given sufficient blood supply, glycolysis is fast and can produce a large amount of ATP rapidly. Moreover, the byproducts of glycolysis can provide carbon sources for cancer cells to synthesize nucleotides, amino acids, and lipids that are essential for the growth of new cancer cells.

The overproduced lactate will need to be transported out of the cell, known as lactate efflux, to forward the biochemical reactions. MCT4, a monocarboxylate transporter primarily responsible for lactate efflux, is overexpressed in prostate cancer. The co-transport of protons and lactate through MCT4 can acidify the extracellular environment and facilitate cancer metastasis [11]. Also, lactate can be taken up by aerobic cancer cells and become an energy source and metabolic intermediate [12]. It has been confirmed that lactate efflux and MCT4 expression are correlated with cancer aggressiveness [13]. High levels of lactate production and efflux are promising indicators for predicting cancer aggressiveness, progression to metastasis, and response to therapy [14] [15] [16]. These findings suggest the promise of lactate metabolism and transport as a biomarker for cancer detection and characterization.

Technical Rationale

The assessment of lactate production and efflux and MCT4 expression has largely relied on the *in vitro* molecular biology tests. Although ^1H magnetic resonance spectroscopy (MRS) can noninvasively detect metabolites such as lactate *in vivo*, the low concentration of lactate and the frequency overlap between lactate and lipids are the main obstacles to acquiring clinically useful data [17]. Fortunately, metabolic magnetic resonance imaging (MRI) with hyperpolarized substrates has enabled real-time measures of enzymatic activity and metabolic shift, and has shown great promise in both pre-clinical [18] and clinical studies [19] as a tool for diagnosis, staging and assessing treatment response of cancer.

Pyruvate is readily hyperpolarized by the Dynamic Nuclear Polarization (DNP) system, and lactate is a proven effective prostate cancer biomarker using hyperpolarized ^{13}C imaging [20]. It has been shown that overall production of lactate converted from hyperpolarized

^{13}C labeled pyruvate correlates with prostate cancer grades in mice [18]. However, previous research has largely focused on measuring the amount of metabolites, such as the overproduction of lactate, but not the transport of metabolites. A few recent studies performed at the UCSF Kurhanewicz Lab have successfully used hyperpolarized ^{13}C diffusion weighted MRI/MRS to rapidly study metabolite compartmentalization in phantoms [21], cells [22], and animals [23]. These studies demonstrated the promise that measuring extra- and intracellular distribution of lactate by hyperpolarized diffusion weighted MRI could reveal the lactate efflux level *in vivo*, thereby improving tumor detection and characterization.

Hypothesis and Study Design

The hypothesis of this project is that hyperpolarized diffusion weighted MRI can assess cancer aggressiveness by providing cancer-specific information about lactate production and efflux/transport, and the microstructural environment of the tumor. By this pilot study, we wanted to evaluate the feasibility of applying hyperpolarized diffusion weighted MRI *in vivo* in prostate cancer, the signal-to-noise ratio (SNR) of images, apparent diffusion coefficients (ADC) fitting quality, and reproducibility as well as reliability of the methods. The core measurement of this study is metabolite ADC mapping. In order to compare the metabolite ADC difference in early- and late-stage tumors, early and late-stage transgenic adenocarcinoma mouse prostate (TRAMP) models were injected with hyperpolarized pyruvate, then imaged by a diffusion weighted sequence. ADC maps of pyruvate and lactate were generated by voxel-wise fitting diffusion weighted signal to a monoexponential decay model. The results were analyzed qualitatively and compared with a previous bioreactor study using similar methods. The metabolite ADCs of early- and late-stage tumors were compared.

Chapter 2

Imaging Theory

2.1 Magnetic Resonance

Nuclear Magnetic Resonance (NMR), first discovered by Isidor Isaac Rabi [24], is a physical phenomenon where nuclear spins receive and emit electromagnetic irradiation or radiofrequencies (RF). All nucleons, including protons and neutrons, have the intrinsic quantum property of *spin* carried by elementary particles. Nuclei with an odd number of protons and/or neutrons, such as ^1H , ^{13}C , ^{31}P , ^{15}N , possess a nuclear spin angular momentum \mathbf{S} . Magnetic dipole momentum, μ , is associated with spin angular momentum \mathbf{S} , and their ratio (μ/\mathbf{S}) is defined as gyromagnetic ratio γ , which is unique for each isotope. The nuclear spins can only precess and resonate at a certain frequency, known as the *Larmor frequency*, ω , depending on the main magnetic field and the magnetic property of the spin, as described by the equation below,

$$\omega = \gamma \cdot B_0 \quad (2.1)$$

where γ is gyromagnetic ratio ($\text{rad}^{-1} \cdot \text{s}^{-1} \cdot \text{T}^{-1}$), and B_0 (T) is external field strength.

In the absence of external magnetic fields, spins are randomly aligned; however, in the presence of external magnetic field B_0 , spins tend to align in the same direction as B_0 and create a net magnetization moment \mathbf{M} , which can be viewed as a vector and the sum of μ in the classic description of NMR.

A quantum mechanical description of NMR helps to explain the magnitude of \mathbf{M} and hyperpolarization. \mathbf{M} exists because of the energy level splitting of non-zero spins through the interaction with B_0 , as described in the *Zeeman Effect* [25]. For spin 1/2 nuclei, such as ^1H and ^{13}C , the energy difference, ΔE , is determined by

$$\Delta E = -\mu \cdot B_0 = h \cdot \frac{\gamma}{2\pi} \cdot B_0 \quad (2.2)$$

where h is Planck's constant ($J \cdot s$). There are two energy sublevels for spin 1/2 nuclei: parallel (n+) and antiparallel (n-). The ratio of two spin energy populations is determined by Boltzmann distribution,

$$\frac{n_-}{n_+} = \exp\left(\frac{-\Delta E}{kT}\right) \quad (2.3)$$

where k is Boltzmann's constant ($J \cdot K^{-1}$) and T is absolute temperature (K). The polarization, P , is defined as the fractional difference between two spin energy populations,

$$P = \frac{n_+ - n_-}{n_+ + n_-} = \tanh \frac{-h\gamma B_0}{2\pi kT} \quad (2.4)$$

As shown in equation 2.4, polarization is determined by spin property (γ), external field strength and temperature; it is very tiny at thermal equilibrium. For instance, at room temperature and 3T, the polarization of ^1H ($\gamma = 4.3\text{MHz/T}$) is 0.001%, and the polarization of ^{13}C ($\gamma = 1.1\text{MHz/T}$) is 0.00026%. This small net difference is the fundamental of net magnetization moment and MR signal.

MRI is an imaging technology based on NMR phenomenon. From a classical perspective, the net magnetization moment can be excited and torqued from its equilibrium through interaction with an electromagnetic field rotating at the *Larmor frequency*, B_1 , also known as radiofrequency (RF) pulse. Following excitation, the magnetization moment continues to precess with the aim of returning to equilibrium; this process is called relaxation. During relaxation, the transverse component of magnetization can be detected by RF coils. The resulting signal will be processed and translated into images. The *Bloch equation* describes the behavior of magnetization moment,

$$\frac{d\mathbf{M}}{dt} = \mathbf{M} \times \gamma \mathbf{B} - \frac{M_x \mathbf{i} + M_y \mathbf{j}}{T_2} - \frac{(M_z - M_0) \mathbf{k}}{T_1} \quad (2.5)$$

where M_x and M_y are transverse magnetizations, M_z is longitudinal magnetization, and i, j, k are vector units. During relaxation, the transverse component of magnetization (M_{xy}) can be detected by RF coils, and the resulting signal can be processed and translated into images.

2.2 Hyperpolarized MR

Carbon forms the backbone structure of organic molecules, including metabolites. ^{13}C MRI can provide metabolic information about biological tissue and disease. However, ^{13}C imaging at thermal equilibrium condition is limited by the low signal-to-noise ratio (SNR) due to the low concentration of metabolites and the relatively small gyromagnetic ratio. Hyperpolarized MRI has emerged as a novel imaging technology that can noninvasively detect metabolic shifts in cancers.

Several hyperpolarization techniques [26] have been developed to increase polarization through perturbing spins from thermal equilibrium and increasing the fraction of parallel spins (n_+). One of most the commonly used hyperpolarization methods, dynamic nuclear polarization (DNP) technique can increase ^{13}C MR signal by 10,000 fold [26]. Generally speaking, there are two sources of hyperpolarization: 1) the low temperature of 1K increases polarization level by 300 folds, and 2) microwave irradiation transfers polarization from electron spins to nuclear spins through “solid effect” and “thermal mixing” [27]. This considerable signal enhancement, along with the chemical shift sensitivity between ^{13}C labeled metabolites, provides the opportunity for direct imaging of metabolites and metabolic process. In cancer imaging, hyperpolarized MR can detect the metabolic reprogramming of cancer cells, therefore improving the diagnosis and characterization of cancer.

2.3 Diffusion and Diffusion MR

The term "diffusion" is often used to describe various molecular and particle movements, although the technical definition is random mass transport process without requiring bulk

motion [28]. Brownian motion refers to the molecular self-diffusion due to thermal energy. Fick's first law explains this phenomenon, written in three dimensions,

$$J = -D\nabla C \quad (2.6)$$

where J is the net flux vector ($mol \cdot mm^{-2} \cdot s^{-1}$), D is diffusion coefficient ($mm^2 \cdot s^{-1}$), and C is the concentration ($mol \cdot mm^{-3}$). The diffusion coefficient, also referred to as diffusivity, is determined by the size and structure of the diffusing molecules, temperature, and microstructure environment.

Diffusion MR can elucidate the microstructure features by incorporating diffusion weighting gradients into the spin echo pulse sequence. Diffusion pulsed gradients are usually placed symmetrically around the 180° refocusing pulse. Therefore, "diffusion" can cause phase dispersion and signal cancelation between spins; whereas stationary spins or spins with low diffusivity experience no or little phase shift and signal cancellation. A more accurate way to describe the principle of diffusion MR is that it sensitizes "translational motion", rather than "diffusion". An apparent diffusion coefficient (ADC) can be generated by fitting the diffusion weighted signal to an exponential decay equation, such as equation 3.1. More technical details about diffusion MR pulse sequence and parameters are described in Chapter 3.

The basic principle of measuring the extra- and intracellular distribution of metabolites by diffusion MR is measuring the ADC of metabolites. This theory is based on prior knowledge that: 1) diffusion of molecules is restricted by the cellular membrane, thus, intracellular molecules have a lower ADC, whereas extracellular molecules have a more free diffusion and much higher ADC; and 2) lactate is produced inside the cells, but can be exported out of cells via MCT4 which is overexpressed in aggressive prostate cancer cells. Therefore, *in vivo* ADC can provide information about the compartmentalization of lactate and pyruvate in the tumor, which reflects lactate production and efflux.

Chapter 3

Methods

3.1 Hardware

All imaging studies were performed on a 14.1 Tesla (T) Varian INOVA spectrometer (600 MHz ^1H /150 MHz ^{13}C), equipped with a 10 mm broadband probe, 100 G/cm gradients, and Vnmrj microimaging system (Agilent Technologies). A dual-tuned $^1\text{H}/^{13}\text{C}$ coil was used to acquire ^1H T2 weighted anatomy images and ^{13}C diffusion weighted images. A dedicated proton coil was used to acquire proton diffusion weighted images.

3.2 Hyperpolarization

Sample preparation and polarization methods are similar to those published previously [26]. The $[1-^{13}\text{C}]$ pyruvate sample was prepared with neat pyruvic acid, 16.5 mM of the trityl radical OX063 (GE Healthcare), and 1.5 mM gadolinium-based contrast agent Dotarem (Guerbet). Dynamic nuclear polarization was performed at either the HyperSense System (Oxford Instruments, Abingdon, UK) which operates at 3.35T, 1.3K and 94.072 GHz microwave irradiation, or at a prototype DNP polarizer which operates at 3.35T, 1.4K and 94.095 GHz microwave irradiation. To compensate for the signal loss due to diffusion weighting and multi-excitation, 48 μL aliquots of $[1-^{13}\text{C}]$ pyruvate, double the amount of what is regularly used, were polarized for at least 90 minutes to increase SNR and polarization. Samples were

rapidly thawed and neutralized to a physiologic pH with a 4.5g buffer solution comprised of 160mM NaOH, Tris buffer and EDTA.

3.3 Animal Experiment and Scan Protocol

Animal studies were performed in accordance with UCSF Institutional Animal Care and Utilization Committee standards. The transgenic adenocarcinoma of the mouse prostate (TRAMP) model is a well-characterized animal model that imitates the human disease progression, histopathological and metabolic changes [29] [30]. Five TRAMP models, including four late stage and one early stage, were used in this study. The tumor grade was estimated by T2 weighted images and proton diffusion weighted images before the hyperpolarized study. Animals were anesthetized with an isoflurane and oxygen mixture and placed on the hot water tubes heated to 37°C. All MR data acquisitions were respiratory gated except for the fast spin echo sequence. 300 μ L neutralized hyperpolarized agents were injected into the animal through the ventral tail vein, immediately after measuring their pH value, at a constant rate within 15 seconds. ^{13}C diffusion weighted images were acquired at 30 or 31s after the start of injection depending on the respiration rate. 1° and 90° spectroscopy were performed on the whole ^{13}C imaging slab before and after the diffusion weighted imaging, respectively.

3.4 ^1H Imaging

All anatomical images were be acquired in axial and coronal planes with a T2-weighted single spin echo sequence and a fast spin echo sequence, using $^{13}\text{C}/^1\text{H}$ dual-tuned transmit/receive coils. ^1H diffusion weighted images were acquired with a pulsed gradient single spin echo sequence to assess tumor condition.

3.5 Hyperpolarized ^{13}C Diffusion Weighted Imaging

Before acquiring diffusion data, flip angle calibrations were performed by measuring the transmitter power required to produce a 180° pulse with a ^{13}C urea phantom. Hyperpolarized ^{13}C diffusion weighted images were acquired using a unipolar pulsed-gradient double spin echo sequence with a single-shot flyback echo-planar imaging (EPI) readout (figure 3.1), prescribed for a 12 mm thick slice and 2 x 2 mm in-plane resolution. The RF pulses consist of a slice-selective excitation pulse followed with a pair of adiabatic refocusing pulses, which is similar to previous ^{13}C spin echo acquisitions [23] [31]. A symmetric-frequency response, single band "true null" spectral spatial pulse was used to alternatively excite $[1-^{13}\text{C}]$ lactate and $[1-^{13}\text{C}]$ pyruvate which have a 1850 Hz chemical shift at 14.1 T. The adiabatic 180° refocusing pulses are insensitive to transmitter-gain calibrations, and can avoid signal loss by realigning the magnetization to B_0 . At the end of each readout, the radiofrequency and gradient spoiling were used to eliminate transverse magnetization. Two diffusion gradient pairs around the refocusing pulses were applied in 3 directions (x, y, and z) to increase diffusion weighting and achieve b-values up to $1000 \text{ s} \cdot \text{mm}^{-1}$. A relatively large slices thickness (12 mm) was used in all ^{13}C scans to achieve sufficient SNR with diffusion weighting. Constant flip angles of 30° were used. Although the diffusion-compensated variable flip angle scheme can consume the nonrenewable hyperpolarized signal and increase SNR at higher b-value, slice profile difference of variable flip angles may increase bias in ADC measurement and interpretation.

In order to improve the accuracy of ADC measurement, an array of 4 b-values = [1000, 600, 300, 25] $\text{s} \cdot \text{mm}^{-1}$ was used in this study. Both pyruvate and lactate were imaged, and 4 scans of different diffusion weighting were performed for each metabolite. $\text{TR} = 0.1\text{s}$, however, due to the respiratory gating, the acquisition time of 4 b-values per metabolite is 3s. Between scans of different diffusion weighting, only gradient amplitude was changed while gradient duration and TE (0.0815s) were kept constant to minimize the T2 weighting differences.

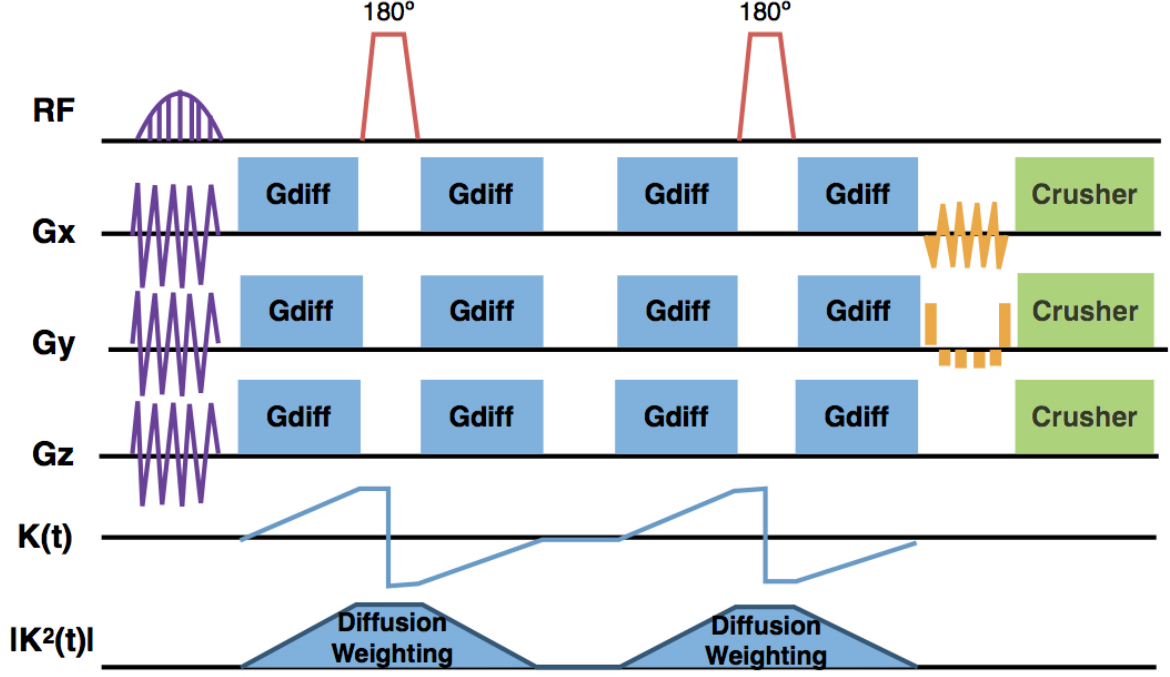


Figure 3.1: Hyperpolarized ^{13}C Diffusion MR pulse sequence diagram

3.6 Data Analysis

ADC maps of each metabolite will be generated by fitting the signal intensity of 4 diffusion weighted images to a monoexponential decay on a voxel-by-voxel basis:

$$S_i = S_0 e^{-b \cdot \text{ADC}} \quad (3.1)$$

where S_i is the diffusion sensitized signal for a certain b-value, and S_0 is the non-diffusion-sensitized signal. The b-values for hyperpolarized ^{13}C scans were determined from numerical integration [32]:

$$b = \int_0^{TE} k^2(t) dt \quad (3.2)$$

where

$$k(t) = \gamma \int_0^t G(t') dt' \quad (3.3)$$

The diffusion weighting is proportional to $|k^2(t)|$ as shown by the shaded area in Figure 3.1.

Flip angle errors can cause significant inaccuracy to ADC measurement of hyperpolarized metabolites [23]. To correct the deviation between the actual and the expected flip angle, a B1 map was created by using the two images with flip angles 45° and 90° and their double angle identity [33]. Moreover, a cos term was added to account for the nonrenewable hyperpolarized magnetization:

$$\frac{S_{n+1}}{S_n} = \frac{\sin(2\theta_n)\cos(\theta_n)}{\sin(\theta_n)} = \frac{2\sin(\theta_n)\cos(\theta_n)\cos(\theta_n)}{\sin(\theta_n)} = 2\cos^2(\theta_n) \quad (3.4)$$

where S_n is the signal from 45° scan and S_{n+1} is the signal from 90° scan. Solving θ_n from equation 3.4 on a voxel-by-voxel basis gives the true flip angle used in the scan. Then the fractional error was derived for each voxel, which was subsequently used to correct the flip angle for each scan on a voxel-by-voxel basis.

The RF utilization's effect on non-renewable hyperpolarized signal needs to be corrected before ADC mapping:

$$S_{n,corr} = \frac{S_{n,acq}}{\sin(\theta_n) \cdot \prod_{k=1}^{n-1} \cos(\theta_k)} \quad (3.5)$$

where n can be 2, 3 and 4.

To examine metabolite ADC fitting quality, residual sum of squares (RSS) was calculate voxel-wise. The region-wise ADC fitting quality was examined by plotting the average signal of diffusion weighted images within the region of interest (ROI) of the tumor and the ADC fit in the same graph. The ROIs were drawn on the axial T2 weighted proton images that are correlated with the ^{13}C images, and cover the whole tumor region. The average metabolite ADC values and standard deviation within ROI were also calculated.

T1 governed hyperpolarization decay is neglected in all calculation due to the short TR used. All data analysis was performed in MATLAB (MathWorks).

Chapter 4

Results

Since this was the first time hyperpolarized ^{13}C diffusion weighted MR sequence was used in TRAMP models at 14T, the acquisition parameters were first optimized. We found that a double dose ($48\ \mu\text{L}$) of pyruvate can increase SNR significantly; 30s - 31s acquisition delay after the injection of hyperpolarized pyruvate can provide better SNR compared to 20s and 40s delay; a maximum b-value of $1000\ \text{s} \cdot \text{mm}^{-1}$ can achieve sufficient diffusion weighting with reasonable SNR for ADC mapping compared to maximum b-value of $2000\ \text{s} \cdot \text{mm}^{-1}$.

One early-stage and four late-stage TRAMP models were studied and included in the group analysis. For each animal, two sets of data were acquired using the same parameters on the same day, and the data set with decent SNR and fitting quality, as measured by RSS, was included in the analysis.

The following images and spectroscopy data were acquired from a representative late stage TRAMP model (MS 391), except as stated otherwise. 1° and 90° ^{13}C spectroscopy were performed on the ^{13}C imaging slab before and after diffusion weighted imaging (DWI) respectively (Figure 4.1). The ratio of lactate and pyruvate increased during the DWI time frame of 6 seconds, as measured by peak height ratio, suggesting that the metabolic flux of pyruvate-to-lactate is rapid and significant in late-stage cancer.

The diffusion weighted images can reflect the metabolic flux of pyruvate-to-lactate, as shown by the high signal intensity of lactate images (Figure 4.2). Generally speaking,

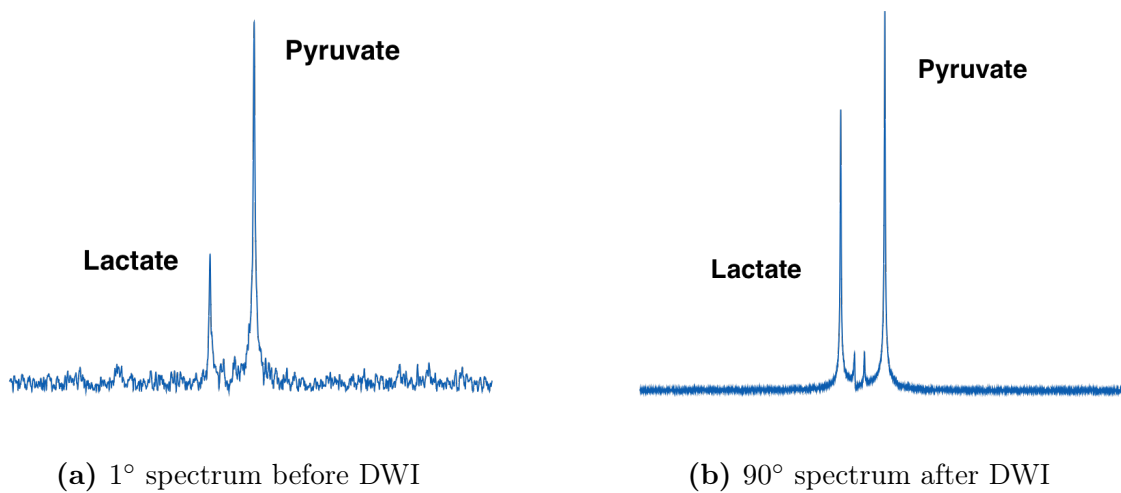


Figure 4.1: ^{13}C MR spectroscopy of the imaging slab

metabolite diffusion weighted images with low b-values have higher signal intensities than those of high b-values.

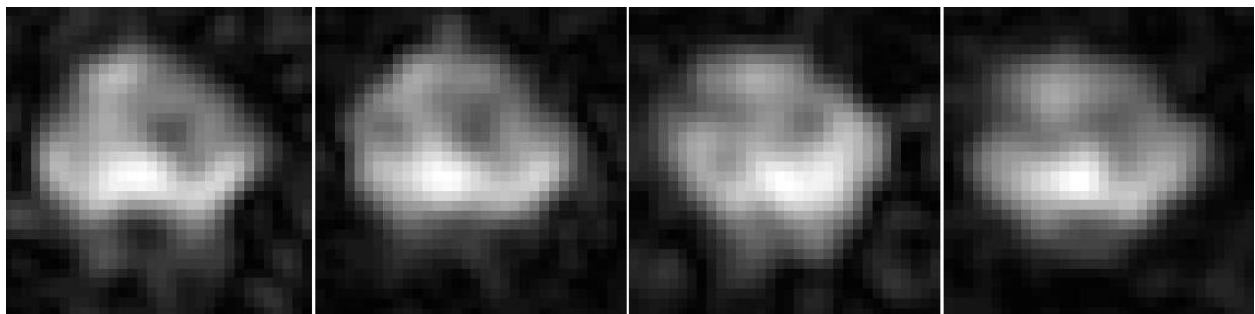


Figure 4.2: Diffusion weighted images of lactate
From left to right, b-values = $[1000, 600, 300, 25] \text{ s} \cdot \text{mm}^{-1}$

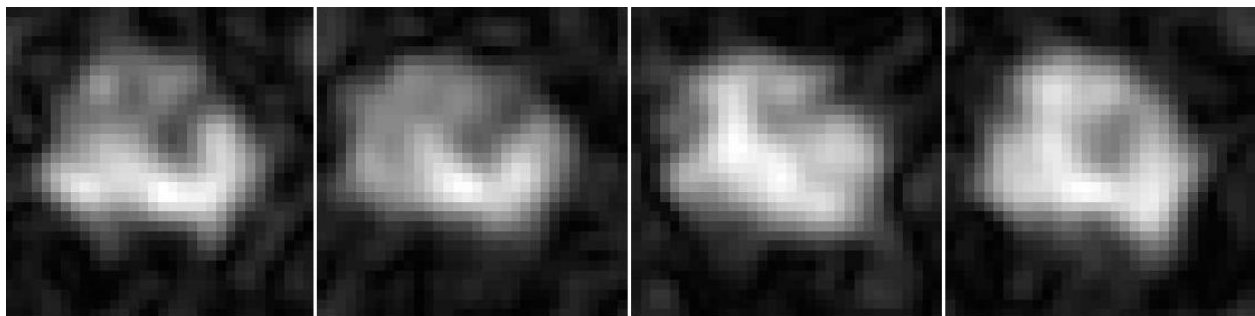


Figure 4.3: Diffusion weighted images of pyruvate
From left to right, b-values = $[1000, 600, 300, 25] \text{ s} \cdot \text{mm}^{-1}$

ADC maps of pyruvate and lactate were overlaid on the axial ^1H anatomical image, as shown in Figure 4.4. While the tumor is heterogeneous, the overall pyruvate ADC is higher than lactate, as represented by yellow-red for pyruvate v.s. dark blue for lactate, indicating differences in metabolite compartmentalization. This can also be seen in the histogram of metabolite ADC maps of the whole tumor region (Figure 4.5). Moreover, pyruvate has more heterogeneous distribution than lactate, suggesting that the compartmentalization of pyruvate is more diverse and complicated than lactate. It can be seen that the ADC fits of monoexponential decay model almost match the actual signal, as shown in Figure 4.6.

The summarized results showed that pyruvate ADC (0.91 ± 0.12) is higher than lactate ADC (0.65 ± 0.91) in late-stage TRAMP. To better understand our findings, we compared our *in vivo* ADC measurement to a previous study on renal cell carcinoma (RCC) bioreactor using similar methods, where complete separation of intra- and extra-cellular signal was achieved [34]. We found that lactate ADCs in TRAMP, regardless of stage, are close to bioreactor extracellular ADC rather than intracellular ADC. Moreover, we found that the ADC for lactate increases by nearly 50% in late-stage tumors compared to the early-stage tumor [0.65 ± 0.11 (n=4) vs. 0.46 (n=1)].

MS 398 had a late-stage tumor that has a representative necrotic region with relatively clear boundary. A case analysis was performed on MS 398 to study the effect of tumor morphology on the metabolite diffusivity, where metabolite ADCs of homogeneous region and necrotic region were compared (Table 4.3). The results showed that the necrotic region had a lower metabolite ADC than in the homogeneous region for both lactate (0.44 ± 0.13 vs. 0.54 ± 0.07) and pyruvate (0.61 ± 0.25 vs. 0.79 ± 0.25). Histograms showed that pyruvate ADCs have more diverse distribution in the homogeneous region than the necrotic region, and lactate ADCs are less diverse in the homogeneous region.

To study the flow effects on the ADC measurement, we performed ADC fitting without the signal of lowest b-value which is the most sensitive acquisition to the flow effect (Table 4.4). We found out that both metabolite ADCs generated without the lowest b-value are

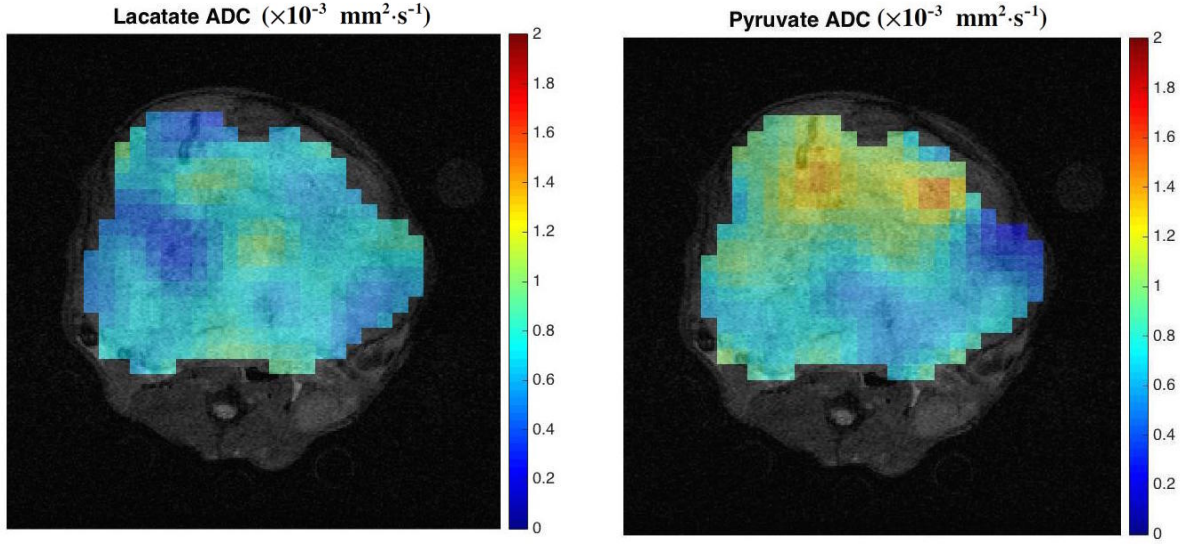


Figure 4.4: Overlay of metabolite ADC maps and T2 weighted anatomy images

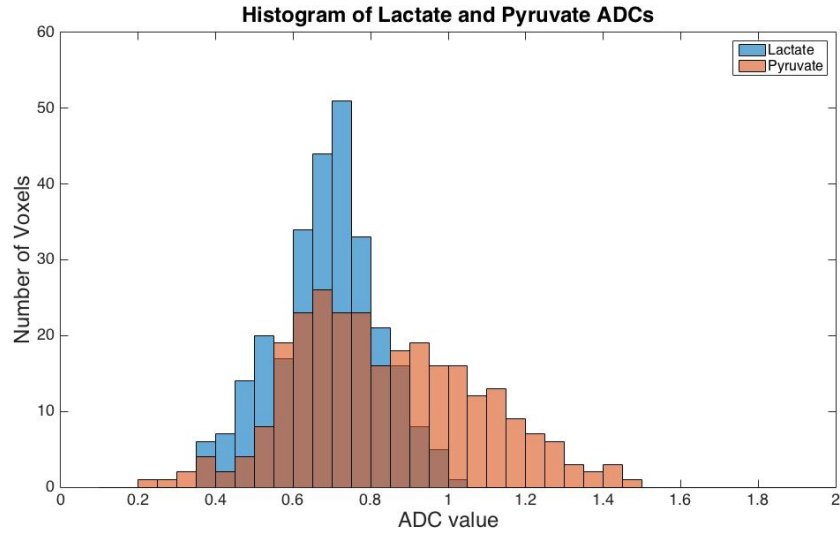


Figure 4.5: Histogram of Metabolite ADC maps

lower than those generated with 4 b-values (lactate: 0.59 ± 0.09 vs. 0.65 ± 0.11 ; pyruvate: 0.89 ± 0.15 vs. 0.91 ± 0.12). It is worth mentioning that we did not include the early-stage TRAMP model into this analysis because the SNR for early-stage tumors are already low and eliminating signal of one b-value could deteriorate the ADC fitting quality.

To assess tumor condition, proton diffusion weighted images were acquired, and ADC

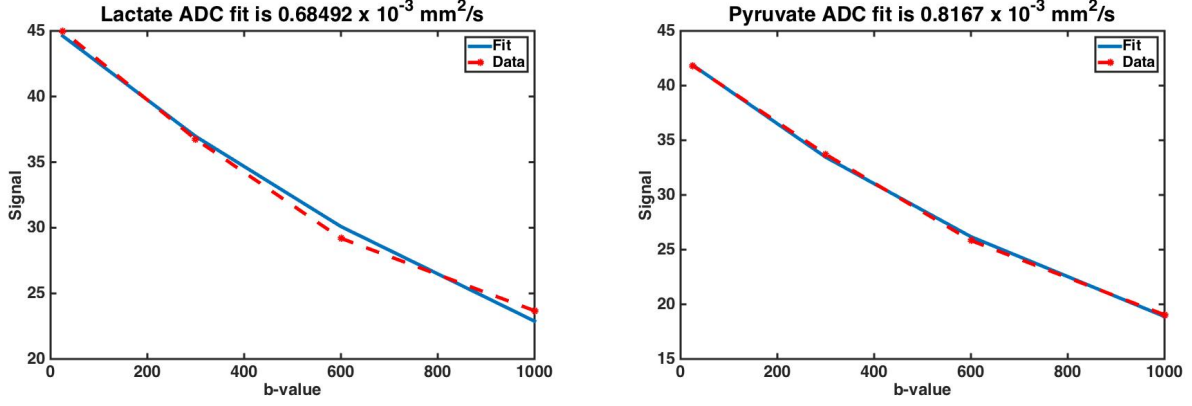


Figure 4.6: Fitting Quality of Metabolite ADC

Table 4.1: *in vivo* effective ADC of metabolites in the prostate tumor

Mean ADC value of Tumor Regions ($\times 10^{-3} \text{ mm}^2 \cdot \text{s}^{-1}$)			
TRAMP Models		Lactate	Pyruvate
Late Stage	MS 381	0.77 ± 0.31	1.04 ± 0.54
	MS 383	0.64 ± 0.22	0.98 ± 0.21
	MS 391	0.68 ± 0.13	0.84 ± 0.24
	MS 398	0.52 ± 0.095	0.77 ± 0.25
Early Stage	MS 392	0.46 ± 0.37	0.85 ± 0.31

Table 4.2: Metabolite ADC comparison: *in vivo* vs. bioreactor

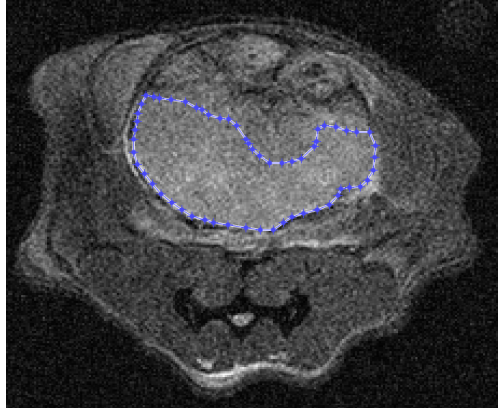
Subjects	ADC	Lactate	Pyruvate
Bioreactor - UOK262	Intracellular	0.19 ± 0.03	0.10 ± 0.007
	Extracellular	0.57 ± 0.10	1.19 ± 0.06
TRAMP - Late Stage	<i>in vivo</i>	0.65 ± 0.11	0.91 ± 0.12
TRAMP - Early Stage	<i>in vivo</i>	0.46	0.85

ADC unit: $\times 10^{-3} \text{ mm}^2 \cdot \text{s}^{-1}$; UOK262 cells are derived from metastatic hereditary leiomyomatosis renal cell carcinoma (HLRCC), a highly aggressive type of cancer[34].

maps were generated using the same method as ¹³C metabolite ADC mapping. We found that proton/water ADC is lower than metabolite ADC, as evidenced by the color-coded ADC map and its histogram (Figure 4.8).

Table 4.3: Metabolite ADC comparison: the effect of tumor morphology

MS 383	Lactate	Pyruvate
Homogeneous Region	0.54 ± 0.07	0.79 ± 0.25
Necrotic Region	0.44 ± 0.13	0.61 ± 0.25
Whole Tumor	0.50 ± 0.11	0.71 ± 0.27



The T2 weighted axial image of MS 398 shows a necrotic late-stage tumor, with a ROI defined as the homogeneous region.

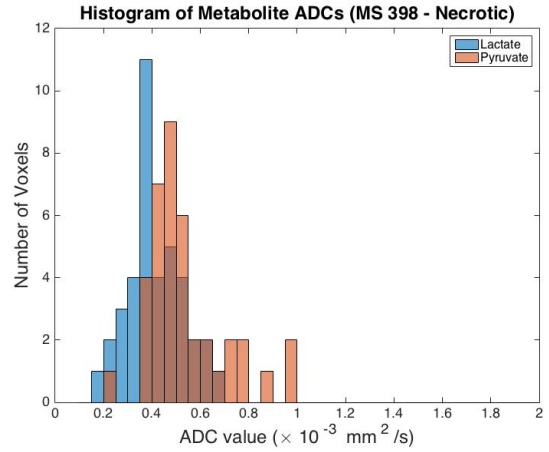
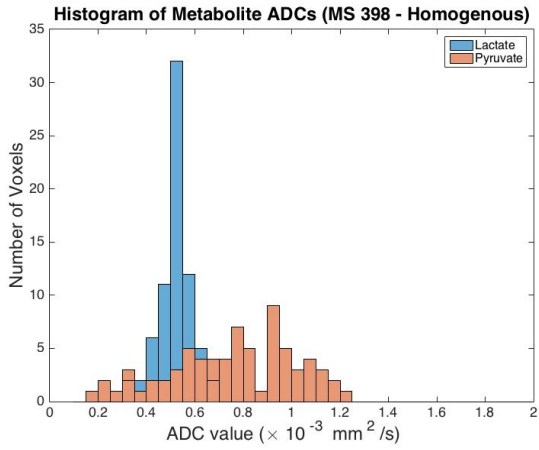


Figure 4.7: A case analysis on the effect of morphology on metabolite diffusivity: histogram of ADC maps.

Table 4.4: *In vivo* metabolite ADC measured without the lowest b-value

Mean ADC value of Tumor Regions ($\times 10^{-3} \text{ mm}^2 \cdot \text{s}^{-1}$)		
TRAMP	Lactate	Pyruvate
MS 381	0.62 ± 0.34	0.92 ± 1.21
MS 383	0.59 ± 0.17	1.06 ± 0.48
MS 391	0.67 ± 0.33	0.86 ± 0.39
MS 398	0.46 ± 0.15	0.71 ± 0.24
Summary	0.59 ± 0.09	0.89 ± 0.15

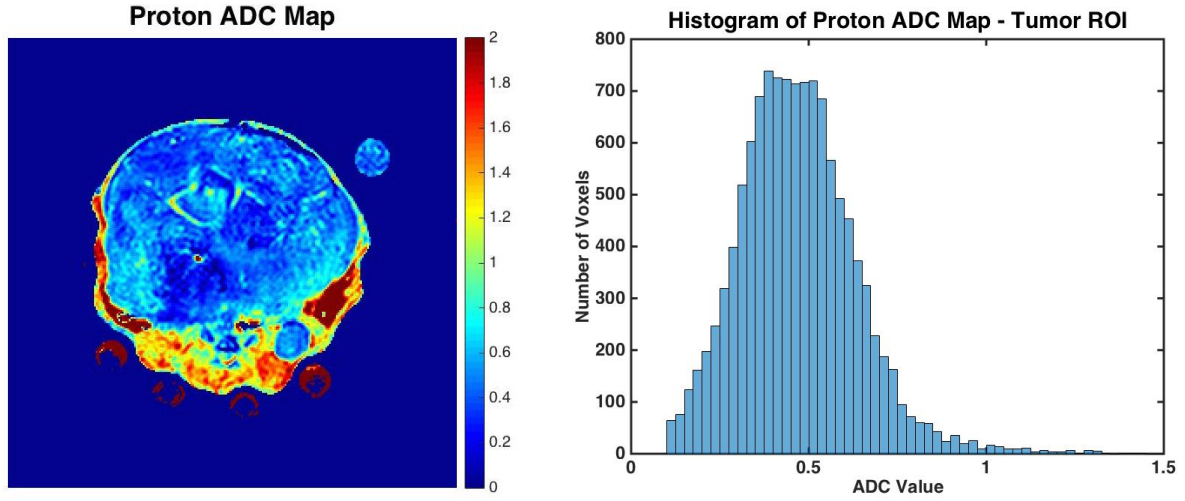


Figure 4.8: Proton ADC map and its histogram

Chapter 5

Discussion

This thesis work is one of the first *in vivo* metabolite diffusion weighted imaging studies using hyperpolarized substrates. Although lactate is produced intracellularly, our results demonstrate that its *in vivo* effective ADC is actually close to the extracellular ADC in bioreactors. This finding suggests that lactate efflux is rapid and appreciable in prostate cancer, and can be detected by hyperpolarized diffusion weighted MRI. On the other hand, pyruvate *in vivo* ADC is lower than its ADC in the bioreactor extracellular space, possibly due to the effects of cellularity. Moreover, we found that lactate ADC in late-stage tumors ($0.65 \pm 0.11 \text{ mm}^2 \cdot \text{s}^{-1}$, n=4) is higher than early-stage ($0.46 \text{ mm}^2 \cdot \text{s}^{-1}$, n=1), indicating there is increased lactate efflux in late-stage cancer. Lactate efflux is a concentration driven passive transport, and it is limited by the expression of MCT4. Our finding is consistent with the fact that late-stage prostate cancer cells overproduce lactate and overexpress MCT4.

We tested the feasibility and reproducibility of *in vivo* hyperpolarized diffusion weighted MRI. Our ADC measurements were in a similar range to previous bioreactor studies. Additionally, we could often achieve consistent results from two experiments on the same animal and the same day. The diffusion weighted images and the histogram of metabolite ADC show that *in vivo* metabolite compartmentalization is heterogeneous, especially for pyruvate. Therefore, ADC mapping by voxel-wise fitting is particularly suitable for hyperpolarized diffusion weighted MRI. The fitting quality was examined by plotting the signal and fit, and

by calculating RSS; and similar fitting quality can be easily achieved on other late-stage TRAMP models, but not on early-stage TRAMP models.

We found that *in vivo* pyruvate ADC is higher than lactate ADC, which is consistent with the findings of previous bioreactor studies. There are several explanations for this phenomenon. Firstly, lactate has more intracellular distribution than pyruvate, causing lactate diffusion is more restricted. Secondly, although lactate and pyruvate have a similar molecular weight, lactate has an extra hydroxyl group and thus is bulkier than pyruvate. Moreover, the hydroxyl group enables lactate to form hydrogen bonds with other eligible molecules, which causes decreased diffusivity.

We hypothesized that pyruvate ADC could elucidate microstructural features of the extracellular space; to be specific, could reflect tumor cellularity via decreased ADC. However, our results show that pyruvate ADC is not lower but slightly higher in late-stage tumors compared to early-stage. Although cellularity is more severe in late-stage tumors, there is also more angiogenesis than early-stage tumors. These newly formed and excessively growing vessels are tortuous and leaky, which in turn contributes to increased overall perfusion. The slight increase of pyruvate ADC in late-stage cancer is possibly caused by enhanced vascular flow and the leafiness of tumor microvasculature. Although there is no particular signal enhancement near the major vasculatures seen on the diffusion weighted images, this finding may suggest that the amount of pyruvate presented in the microvasculature is not negligible. On the other hand, cellularity is a confounding variable for lactate ADC interpretation. Currently, proton DWI and ADC mapping can assess cellularity qualitatively. Possibly in the future quantitative assessment of cellularity's effect on lactate ADC can be achieved.

It is challenging to find the optimum b-values for hyperpolarized diffusion weighted MRI because of the dynamic nature of metabolism and the nonrenewable nature of the hyperpolarized signal. Flow is the net movement of molecules, which is *bulk motion* and a faster movement than diffusion; therefore, it can cause greater signal cancelation and outweigh the true "diffusion" weighting. In order to avoid the flow effect, b-value=0 was not included

in the diffusion weighted MRI acquisition because low b-value is sensitive to fast movements, such as flow. However, the fact that ADCs generated without the lowest b-value ($25 \text{ s} \cdot \text{mm}^{-1}$) are lower than ADCs generated with all 4 b-values suggests flow effects still exist in our diffusion weighted signal. Another concern regarding our b-value setting is that the maximum b-value ($1000 \text{ s} \cdot \text{mm}^{-1}$) is not high enough to sensitize intracellular diffusion. Especially given that the *in vivo* ADC measured in our study is close to bioreactor extracellular ADC, one may argue this is simply because our sequence can only sensitize extracellular diffusion.

Morphological changes in the tumors may also affect the diffusivity of metabolites. In the comparison of metabolite ADCs of the homogeneous tumor region with the necrotic region, we found that the necrotic region had a lower ADC for both metabolites. Necrosis happens on the basis of imbalance between the demand and supply of energy and nutrition at the cellular level and is an indicator of poor perfusion status. Also, the loss of viable tissues, increased extracellular medium density due to membrane breakdown, fibrosis and steatosis of the necrotic region can hinder the translational motion of metabolites.

There are several major factors affecting *in vivo* molecular translational movement: temperature, molecular structure/interaction, concentration gradient (C in equation 2.6) and microstructural environment. It is still not clear why water ADC is lower than metabolite ADC *in vivo*, given that water has a smaller molecule size. Either a combination of these factors or the acquisition errors caused our observations. However, there is some fundamental difference between water and metabolite diffusion. From a physics perspective, water diffusion is self-diffusion while metabolite diffusion is mixed diffusion. The much greater *in vivo* metabolite concentration gradients may facilitate the *Brownian motion* of metabolites, whereas the concentration gradient plays a lesser role in water diffusion.

Hyperpolarized ^{13}C imaging techniques share some common drawbacks, such as coarse spatial resolution, large thickness, and time restriction. Besides those, there are several challenges for applying hyperpolarized diffusion weighted MRI *in vivo*. Firstly, unlike bioreactor or phantom studies, the delivery of hyperpolarized agents are constrained by the

animal’s condition, such as perfusion status and tumor volume. Secondly, the respiratory and involuntary movement of the animal subject can introduce errors into the data acquisition since diffusion weighted MRI is designed to detect the translational motion of molecules; even though we used respiratory gating, the effect is far from being perfect. Thirdly, current technology cannot separate the *bulk motion*, such as flow and cellular transport, from diffusion or *Brownian motion*. Metabolites are still being transported across membranes and circulating in the vasculature while diffusion gradients are on, which may complicate our data acquisition and ADC measurement. This limitation is also true for conventional proton diffusion. Applying lactate suppression outside of the imaging slab can help to eliminate the effect of circulating lactate that is produced by other organs.

A major limitation of this study is the small sample volume, especially for early-stage tumors: most of our findings are inconclusive. It was difficult to acquire diffusion weighted images with reasonable SNR on early-stage TRAMP model due to the low metabolism and small tumor volume. Moreover, diffusion weighted signal and ADC measurement is very sensitive to acquisition errors and analysis bias; thus, many of the changes we observed might be caused by our measurements rather than the biological changes. Another major limitation is the fuzziness about ADC interpretation. ADC is a physical measurement that can be affected by many biological parameters, including microdynamics and microstructures; its biological significance requires further investigation.

Further efforts will focus on improving the SNR for early-stage tumors, and achieving more precise compartmentalization of metabolites, and a better understanding of measured metabolite ADC. For example, adding hyperpolarized urea will allow us to study perfusion status of the tumor. A larger sample volume is needed to draw conclusions on the metabolite ADC difference between early- and late-stage cancer. Histological analysis of the tumor will be performed, including pathology index and MCT4 expression; then their correlation with the imaging study will be examined.

Chapter 6

Conclusion

We proposed a novel metabolic imaging technique, hyperpolarized diffusion weighted MRI, to study enzyme kinetics and transporter expression *in vivo*, and successfully acquired data on five TRAMP models. The measured metabolite ADC provided an insight into the localization of metabolites. This study serves as one of the first attempts of *in vivo* validation of lactate efflux theory. Moreover, it has been found that lactate ADC is higher in late-stage than early-stage tumors, which is consistent with the overexpression of MCT4 and increased lactate efflux in aggressive cancer.

In conclusion, we demonstrated that hyperpolarized diffusion MRI can study metabolite compartmentalization which can reveal lactate efflux level *in vivo*, and potentially provide insight into MCT4 expression in murine prostate tumors. This technique has shown great promise in assessing cancer aggressiveness and therapeutic responses in a rapid, non-invasive manner.

Bibliography

- [1] Rebecca L Siegel, Kimberly D Miller, and Ahmedin Jemal. Cancer statistics, 2015. *CA: a cancer journal for clinicians*, 65(1):5–29, 2015.
- [2] National Cancer Institute. Seer stat fact sheets: Prostate cancer. <http://seer.cancer.gov/statfacts/html/prost.html>, 2015. [Online; accessed 25-June-2015].
- [3] Ruth Etzioni, David F Penson, Julie M Legler, Dante di Tommaso, Rob Boer, Peter H Gann, and Eric J Feuer. Overdiagnosis due to prostate-specific antigen screening: lessons from us prostate cancer incidence trends. *Journal of the National Cancer Institute*, 94(13):981–990, 2002.
- [4] American Cancer Society. Survival rates for prostate cancer. <http://www.cancer.org/cancer/prostatecancer/detailedguide/prostate-cancer-survival-rates>, 2015. [Online; accessed 30-June-2015].
- [5] Ian Thompson, James Brantley Thrasher, Gunnar Aus, Arthur L Burnett, Edith D Canby-Hagino, Michael S Cookson, Anthony V D’Amico, Roger R Dmochowski, David T Eton, Jeffrey D Forman, et al. Guideline for the management of clinically localized prostate cancer: 2007 update. *The Journal of urology*, 177(6):2106–2131, 2007.
- [6] Patricia A Ganz, John M Barry, Wylie Burke, Nananda F Col, Phaedra S Corso, Everett Dodson, M Elizabeth Hammond, Barry A Kogan, Charles F Lynch, Lee Newcomer, et al.

- National institutes of health state-of-the-science conference: role of active surveillance in the management of men with localized prostate cancer. *Annals of internal medicine*, 156(8):591–595, 2012.
- [7] Kirk A Keegan, Marc A Dall’Era, Blythe Durbin-Johnson, and Christopher P Evans. Active surveillance for prostate cancer compared with immediate treatment. *Cancer*, 118(14):3512–3518, 2012.
- [8] Robert A Gatenby and Robert J Gillies. Why do cancers have high aerobic glycolysis? *Nature Reviews Cancer*, 4(11):891–899, 2004.
- [9] Otto Warburg. On the origin of cancer cells. *Science*, 123(3191):309–314, 1956.
- [10] Matthew G Vander Heiden, Lewis C Cantley, and Craig B Thompson. Understanding the warburg effect: the metabolic requirements of cell proliferation. *science*, 324(5930):1029–1033, 2009.
- [11] A Halestrap and N Price. The proton-linked monocarboxylate transporter (mct) family: structure, function and regulation. *Biochem. J*, 343:281–299, 1999.
- [12] Gregg L Semenza. Tumor metabolism: cancer cells give and take lactate. *The Journal of clinical investigation*, 118(12):3835, 2008.
- [13] Nelma Pérttega-Gomes and Fátima Baltazar. Lactate transporters in the context of prostate cancer metabolism: What do we know? *International journal of molecular sciences*, 15(10):18333–18348, 2014.
- [14] Liem Minh Phan, Sai-Ching Jim Yeung, and Mong-Hong Lee. Cancer metabolic reprogramming: importance, main features, and potentials for precise targeted anti-cancer therapies. *Cancer biology & medicine*, 11(1):1, 2014.
- [15] Stefan Walenta, Michael Wetterling, Michael Lehrke, Georg Schwickert, Kolbein SundfØr, Einar K Rofstad, and Wolfgang Mueller-Klieser. High lactate levels predict likelihood of

- metastases, tumor recurrence, and restricted patient survival in human cervical cancers. *Cancer research*, 60(4):916–921, 2000.
- [16] Kelly M Kennedy and Mark W Dewhirst. Tumor metabolism of lactate: the influence and therapeutic potential for mct and cd147 regulation. *Future Oncology*, 6(1):127–148, 2010.
- [17] May-Britt Tessem, Mark G Swanson, Kayvan R Keshari, Mark J Albers, David Joun, Z Laura Tabatabai, Jeffry P Simko, Katsuto Shinohara, Sarah J Nelson, Daniel B Vigneron, et al. Evaluation of lactate and alanine as metabolic biomarkers of prostate cancer using 1h hr-mas spectroscopy of biopsy tissues. *Magnetic Resonance in Medicine*, 60(3):510–516, 2008.
- [18] Mark J Albers, Robert Bok, Albert P Chen, Charles H Cunningham, Matt L Zierhut, Vickie Yi Zhang, Susan J Kohler, James Tropp, Ralph E Hurd, Yi-Fen Yen, et al. Hyperpolarized ^{13}C lactate, pyruvate, and alanine: noninvasive biomarkers for prostate cancer detection and grading. *Cancer research*, 68(20):8607–8615, 2008.
- [19] Sarah J Nelson, John Kurhanewicz, Daniel B Vigneron, Peder EZ Larson, Andrea L Harzstark, Marcus Ferrone, Mark van Criekinge, Jose W Chang, Robert Bok, Ilwoo Park, et al. Metabolic imaging of patients with prostate cancer using hyperpolarized $[1-^{13}\text{C}]$ pyruvate. *Science translational medicine*, 5(198):198ra108–198ra108, 2013.
- [20] Kayvan R Keshari, Renuka Sriram, Mark Van Criekinge, David M Wilson, Zhen J Wang, Daniel B Vigneron, Donna M Peehl, and John Kurhanewicz. Metabolic reprogramming and validation of hyperpolarized ^{13}C lactate as a prostate cancer biomarker using a human prostate tissue slice culture bioreactor. *The Prostate*, 73(11):1171–1181, 2013.
- [21] Bertram L Koelsch, Kayvan R Keshari, Tom H Peeters, Peder EZ Larson, David M Wilson, and John Kurhanewicz. Diffusion mr of hyperpolarized ^{13}C molecules in solution. *Analyst*, 138(4):1011–1014, 2013.

- [22] Renuka Sriram, Mark Van Criekinge, Ailin Hansen, Zhen J Wang, Daniel B Vigneron, David M Wilson, Kayvan R Keshari, and John Kurhanewicz. Real-time measurement of hyperpolarized lactate production and efflux as a biomarker of tumor aggressiveness in an mr compatible 3d cell culture bioreactor. *NMR in Biomedicine*, 28(9):1141–1149, 2015.
- [23] Bertram L Koelsch, Galen D Reed, Kayvan R Keshari, Myriam M Chaumeil, Robert Bok, Sabrina M Ronen, Daniel B Vigneron, John Kurhanewicz, and Peder EZ Larson. Rapid in vivo apparent diffusion coefficient mapping of hyperpolarized ^{13}C metabolites. *Magnetic Resonance in Medicine*, 2014.
- [24] S Millman, II Rabi, and JR Zacharias. On the nuclear moments of indium. *Physical Review*, 53(5):384, 1938.
- [25] C. Dean. Zeeman splitting of nuclear quadrupole resonances. *Phys. Rev.*, 96:1053–1059, Nov 1954.
- [26] Jan H Ardenkjær-Larsen, Björn Fridlund, Andreas Gram, Georg Hansson, Lennart Hansson, Mathilde H Lerche, Rolf Servin, Mikkel Thaning, and Klaes Golman. Increase in signal-to-noise ratio of $> 10,000$ times in liquid-state nmr. *Proceedings of the National Academy of Sciences*, 100(18):10158–10163, 2003.
- [27] Jan Henrik Ardenkjær-Larsen, S Macholl, and H Johannesson. Dynamic nuclear polarization with trityls at 1.2 k. *Applied Magnetic Resonance*, 34(3-4):509–522, 2008.
- [28] Peter J Basser and Evren Ozarslan. Introduction to diffusion mr. *Diffusion MRI: From quantitative measurement to in-vivo neuroanatomy*, 2009.
- [29] Jeffrey R Gingrich, Roberto J Barrios, Ronald A Morton, Brendan F Boyce, Francesco J DeMayo, Milton J Finegold, Roxani Angelopoulou, Jeffrey M Rosen, and Norman M Greenberg. Metastatic prostate cancer in a transgenic mouse. *Cancer research*, 56(18):4096–4102, 1996.

- [30] Paula J Kaplan-Lefko, Tsuey-Ming Chen, Michael M Ittmann, Roberto J Barrios, Gustavo E Ayala, Wendy J Huss, Lisette A Maddison, Barbara A Foster, and Norman M Greenberg. Pathobiology of autochthonous prostate cancer in a pre-clinical transgenic mouse model. *The Prostate*, 55(3):219–237, 2003.
- [31] Charles H Cunningham, Albert P Chen, Mark J Albers, John Kurhanewicz, Ralph E Hurd, Yi-Fen Yen, John M Pauly, Sarah J Nelson, and Daniel B Vigneron. Double spin-echo sequence for rapid spectroscopic imaging of hyperpolarized ^{13}C . *Journal of magnetic resonance*, 187(2):357–362, 2007.
- [32] Matt A Bernstein, Kevin F King, and Xiaohong Joe Zhou. *Handbook of MRI pulse sequences*. Elsevier, 2004.
- [33] EK Insko and L Bolinger. Mapping of the radiofrequency field. *Journal of Magnetic Resonance, Series A*, 103(1):82–85, 1993.
- [34] Bertram L. Koelsch. *Development of diffusion weighted magnetic resonance acquisition techniques for hyperpolarized carbon-13 metabolites and applications to cancer detection and characterization*. PhD thesis, University of California, San Francisco, June 2014.

Publishing Agreement

It is the policy of the University to encourage the distribution of all theses, dissertations, and manuscripts. Copies of all UCSF theses, dissertations, and manuscripts will be routed to the library via the Graduate Division. The library will make all theses, dissertations, and manuscripts accessible to the public and will preserve these to the best of their abilities, in perpetuity.

Please sign the following statement:

I hereby grant permission to the Graduate Division of the University of California, San Francisco to release copies of my thesis, dissertation, or manuscript to the Campus Library to provide access and preservation, in whole or in part, in perpetuity.

Henry Qm 秦静明
Author Signature

9/9/2015
Date